

Comments to the Author:

Dear Dr Kirilova,

Thanks for the submission of your revised manuscript and supplementary material, which I have read carefully.

I would like to remind you that the choice of the appropriate reviewer lies with the topical editor, and the choice of Dr Gilgannon was entirely justified, irrespective of the fact that he used to work in my group. I would also like to emphasise that Dr Gilgannon has contributed two extremely constructive reviews, both of which were available to you through the MS records website (the latter on August 6).

I understand that you feel that the review process focussed overly on technicalities, however, as described in SE's review criteria (https://www.solid-earth.net/peer_review/review_criteria.html), before a manuscript can be accepted for publication, the scientific methods presented there must be [...] clearly outlined (4), and the description of your work must be sufficiently complete to allow reproduction (5). I am satisfied that this is now the case, and will recommend your manuscript for publication pending a minor technical addition:

Given that you have chosen four substantially different threshold intervals for four different uCT datasets (DFDP-1B 69_2.54: 0 to 28; DFDP-1B 69_2.57: 0 to 44; DFDP-1B 58_1.9: 0 to 74; DFDP-1B 69_2.48: 0 to 46), I would ask you to include screenshots for all four samples with the segmented porosity highlighted (as you did for your sample DFDP-1B 69_2.54 in your rebuttal letter) in the supplementary material. I would ask you to further include the grey value histograms, showing the threshold value, with this figure.

Lastly, as I have done already in email exchanges with your coauthors Toy and Renard, I would like to apologize for the slightly irritating tone of my last communication.

With kind regards,
Florian Fusseis

Dear Dr. Fusseis,

Thank you for the time you spent reviewing our manuscript. As requested, we have added one figure with four screenshots in the supplementary material section.

Kind Regards,

Martina Kirilova

On behalf of co-authors: Virginia Toy, Katrina Sauer, François Renard, Klaus Gessner, Richard Wirth, Xianghui Xiao, and Risa Matsumura

1 Micro- and nano-porosity of the active Alpine Fault zone, New 2 Zealand

3 Martina Kirilova^{1,2}, Virginia Toy^{1,2}, Katrina Sauer¹, François Renard^{3,4}, Klaus Gessner^{5,6}, Richard Wirth^{7,6},
4 and Xianghui Xiao^{7,8,9,10}, and Risa Matsumura²

5 ¹Institut für Geowissenschaften, Johannes Gutenberg Universität Mainz, J. J. Becher Weg 21D-55128, Mainz,
6 Germany

8 Department of Geology, University of Otago, PO Box 56, Dunedin 9054, New Zealand

9 ²Institut für Geowissenschaften, Johannes Gutenberg Universität Mainz, J. J. Becher Weg 21D-55128, Mainz,
10 GermanyDepartment of Geology, University of Otago, PO Box 56, Dunedin 9054, New Zealand

11 ³Department of Geosciences, The Njord Centre¹¹, University of Oslo, Oslo 0316, Norway.

12 ⁴Université Grenoble Alpes, Université Savoie Mont Blanc, CNRS, IRD, IFSTTAR, ISTerre, BP53, 38041
13 Grenoble, France.

14 ⁵Geological Survey of Western Australia, 100 Plain Street, East Perth, WA 6004, Australia.

15 ⁶School of Earth Sciences, The University of Western Australia, 35 Stirling Highway, Crawley, WA 6009

16 ⁶7Helmholtz-Zentrum Potsdam, GFZ, Sektion 4.3, Telegrafenberg, 14473 Potsdam, Germany

17 ⁷8Advanced Photon Source, Argonne National Laboratory, Lemont, IL 60439, USA

18 ⁸9National Synchrotron Light Source II, Brookhaven National Laboratory, Upton, NY 11973, USA

19 *Correspondence to:* Martina Kirilova (martina.kirilova@uni-mainz.de)

20 Abstract

21 Porosity reduction in rocks from a fault core can cause ~~fluid overpressure~~¹²elevated pore fluid pressures, and
22 consequently influence the recurrence time of earthquakes. We investigated the porosity distribution in the New
23 Zealand's Alpine Fault core in samples recovered during the first phase of the Deep Fault Drilling Project (DFDP-
24 1B) by using two-dimensional nanoscale and three-dimensional microscale imaging. Synchrotron X-ray
25 microtomography-derived analyses of open pore spaces show total microscale porosities in the range of 0.1¹³~~to~~
26 0.244%. These pores have mainly non-spherical, elongated, flat shapes and show subtle bipolar orientation.
27 Scanning and¹⁴Transmission electron microscopy imaging¹⁵reveals the samples' microstructural organization,
28 where~~that~~¹⁶ nanoscale pores ornament grain boundaries of the gouge material, especially clay minerals. Our data
29 implies¹⁷ that: (i) the porosity of the fault core is very small and not connected, (ii) the distribution of clay minerals
30 controls the shape and orientation of the associated pores; (iii) porosity was reduced due to pressure solution
31 processes; and (iv) mineral precipitation in fluid-filled pores can affect the mechanical behaviour of the Alpine
32 Fault by decreasing the already critically low total porosity of the fault core, causing elevated pore fluid
33 pressures~~fluid overpressure~~¹⁸, and/or introducing weak mineral phases, and thus lowering the overall fault frictional
34 strength. We conclude that the current state of very low porosity in the Alpine Fault core is likely to play a key role
35 in the initiation of the next fault rupture.

36 **1. Introduction**

37 Fault mechanics, fault structure and fluid flow properties of damaged fault rocks are intimately related (e.g. Gratier
38 and Gueydan, 2007; Faulkner et al., 2010). Fault rupture is associated with intense brittle fracturing that enhances
39 porosity, and thus permeability, and therefore also possible rates and directions of fluid propagation within fault
40 zones (e.g. Girault et al., 2018). Conversely, post seismic recovery mechanisms (gouge compaction and pressure
41 solution processes) result in reductions of porosity, permeability and fluid flow propagation reductions (Renard et al,
42 2000; Faulkner et al., 2010; Sutherland et al., 2012). These processes may cause elevated pore fluid pressures within
43 fault cores, and trigger frictional failure (e.g. Sibson, 1990; Gratier et al., 2003; Zhu et al., 2020). Therefore, the state
44 of porosity within rocks from fault cores can play a key role in fault slip.

45 The Alpine Fault of New Zealand is late in its seismic cycle (Cochran et al., 2017), so studying it allows us to
46 investigate pre-earthquake conditions that may influence earthquake nucleation and rupture processes. Recently,
47 drilling operations were undertaken in this fault zone to investigate the *in situ* conditions (Sutherland et al, 2012,
48 2017). Slug tests in the DFDP-1B borehole (Sutherland et al., 2012) and laboratory permeability measurements of
49 core samples (Carpenter et al., 2014) indicate permeability decreases by six orders of magnitude with increasing
50 proximity to the fault. Furthermore, Sutherland et al. (2012) documented a 0.53 MPa fluid pressure difference across
51 the principal slip zone (PSZ) of the fault, which suggests that the fault core has significantly lower permeability than
52 the surrounding cataclasite units. It is therefore interpreted to act as a fault seal that limits fluid circulation within its
53 hanging wall (Sutherland et al., 2012). Permeability variations like this are closely associated with the porosity
54 evolution of fault cores, and thus are likely to affect the fault strength and seismic properties (Sibson, 1990; Renard
55 et al., 2000; Gratier and Gueydan, 2007).

56 In this study, we investigate the porosity distribution in rocks from the Alpine Fault core and consider the potential
57 effects of this porosity on fault strength. We have measured open pore spaces in these rocks from X-ray computed
58 tomography (XCT) datasets and examined pore morphology by implementing quantitative shape analyses.
59 Lithological and microstructural characteristics of these samples were performed by and using scanning electron
60 microscopy (SEM) and transmission electron microscopy (TEM).

61 **2. Geological setting**

62 New Zealand's Alpine Fault (Fig. 1a) is a major active crustal-scale structure that ruptures in a large earthquake
63 every 291 ± 23 years, the last one of which occurred in 1717 (Cochran et al., 2017). The fault is the main constituent
64 of the oblique transform boundary between the Australian Plate and the Pacific Plate, accommodating around 75%
65 of the relative plate motion. Ongoing dextral strike-slip at 27 ± 5 mm yr⁻¹ along the fault has resulted in a total
66 strike-separation of ~ 480 km over the last 25 Ma (Norris and Cooper, 1995, 2001; Norris and Toy, 2014). In
67 Neogene time, a dip-slip component added to the fault motion has resulted in more than 20 km of vertical uplift of
68 the hanging wall (Norris and Cooper, 1995, 2001; Norris and Toy, 2014). Consequently, rocks comprising the
69 hanging wall of the fault have been exposed in various outcrops, where they can be studied in detail. The
70 amphibolite facies Alpine Schist is the metamorphic protolith of a ~ 1 km thick mylonite zone, which has been
71 exhumed from depth and now structurally overlies an up to 50 m thick zone of brittlely deformed cataclasites and
72 gouges (e.g. Norris and Cooper, 1995, 2001; Norris and Toy, 2014). These rocks have been investigated in outcrops
73 and from samples collected in three boreholes during the two phases of the Deep Fault Drilling Project (DFDP-1A,
74 DFDP-1B and DFDP-2B; Fig. 1a) along the Alpine Fault (Sutherland et al., 2012; Toy et al., 2015; Toy et al., 2017).

75 Most of the brittle shear displacement along the fault has been accommodated within the fault core, which includes
76 Principal Slip Zone (PSZ) gouges and cataclasite-series rocks (Toy et al., 2015). Both in surface outcrops and drill
77 core samples, the Alpine Fault manifests as a thin (5 to 20 cm thick) gouge zone with a predominantly random fabric
78 of clay-rich material (Toy et al., 2015; Schuck et al., 2020). This cohesive but uncemented layer has a significantly
79 finer-grain size significantly finer than the surrounding cataclasite units, which shows that the material was reworked
80 only within this layer, most probably as a result of ultra-communition due to multiple shear events under brittle

81 conditions (Boulton et al., 2012; Toy et al., 2015). The local presence of authigenic smectite clays (Schleicher et al.,
82 2015) and calcite and/or chlorite mineralization within sealed fractures and in the gouge matrix (Williams et al.,
83 2017) indicate that mineral reactions are restricted to an alteration zone within the fault core (Sutherland et al., 2012;
84 Schuck et al., 2020). The Alpine Fault core has been interpreted to have formed during a cyclical history of
85 mineralization, shear, and fragmentation (Toy et al., 2015). In addition, in the DFDP-1B borehole (Fig. 1b,
86 Sutherland et al., 2012) fault gouges occur at two distinct depths: 128.1 m (PSZ-1) and 143.85 m (PSZ-2), which
87 shows that the slip was not localized within a single gouge layer (Toy et al., 2015).

88 3. Sample description and analytical methods

89 3.1 Samples

90 Porosity analyses were performed on four samples representing PSZ gouges and cataclasites of the Alpine Fault
91 core, which were recovered from the DFDP-1B borehole (Fig. 1b, c; Sutherland et al., 2012). These are DFDP-1B
92 58_1.9, DFDP-1B 69_2.48, DFDP-1B 69_2.54 and DFDP-1B 69_2.57. Sample nomenclature includes drill core run
93 number, section number, and centimeters measured from the top of each section. These samples were recovered
94 from drilled depth of 126.94 m, 143.82 m, 143.88 m and 143.91 m, respectively.

95 Detailed lithological and microstructural descriptions of the DFDP-1B drill core were carried out simultaneously
96 with, and after the drilling operations by the DFDP-1 Science Team, and these data were later summarized by Toy et
97 al. (2015). Samples DFDP-1B 58_1.9 and DFDP-1B 69_2.48 belong to foliated cataclasite units (Fig. 1b, c; Toy et
98 al., 2015). These were described as ultracataclasites with gouge-filled shear zones located above PSZ-1 and PSZ-2
99 respectively. Sample DFDP-1B 69_2.54 represents the gouge layer that defines PSZ-2, whereas sample DFDP-1B
100 69_2.57 is composed of brown ultracataclasites that belong to the lower cataclasite unit (Fig. 1b, c; Toy et al., 2015).

101

102 3.2 X-ray computed tomography (XCT)

103 We imaged the samples using X-ray absorption tomography, where the signal intensity depends on how electron
104 density and bulk density attenuate a monochromatic X-ray along its path through the material (e.g. Fusseis et al.
105 2014). We acquired the X-ray microtomography data for this study at the 2-BM beamline of the Advanced Photon
106 Source, Argonne National Laboratories USA in December 2012. The non-cylindrical samples of ~7 mm height and
107 ~ 4 mm diameter were mostly drilled parallel to the foliation, and mounted on a rotary stage, and imaged with a
108 beam energy of 22.50 keV. A charge-couple device camera collected images at 0.25° rotation steps over 180° at a sample-detector distance of 70 mm and yielded a field-of-view of 2.81 mm. The voxel size (i.e. spatial sampling)
109 was 1.3 µm and the spatial resolution was likely in the range between two and three times the voxel size. We
110 have reconstructed the datasets with a filtered back-projection parallel beam reconstruction into 32-bit gray level
111 volumes consisting of 2083_2048 * 2083_2048 * 2083_2048 voxels using X-TRACT (Gureyev et al., 2011).

113 3.3 Analyses of XCT datasets

114 Data analyses and image processing were performed using the commercial software package Avizo 9.1TM (Fig. 2).
115 Initially, the datasets were rescaled to 8-bit grey scale volumes for enhanced computer performance. In addition,
116 small volumes of interest were cropped from the whole volume before a non-local means filter was applied to
117 reduce noise (Buades et al., 2005). For each voxel, this filter compares the value of this voxel with all neighboring
118 voxels in a given search window. A similarity between the neighbors determines a correction applied to each voxel
119 (e.g. Thomson et al., 2018).

120 On the filtered gray-scale images, pores were identified as disconnected materials of as porosity was identified as
121 the darkest phase grey-scale range (Fig. 2a, Supplementary material 1: Fig. 1). The corresponding gray-scale values
122 were thresholded, and the datasets were converted into binary form. This step is called segmentation. Several

123 segmentation techniques exist, from thresholding at a given gray scale value (e.g. Ianossov et al., 2009; Andrewä et
124 al., 2013) to deep learning algorithms (Ma et al., 2020). The choice of oneIt is up to the user to choose the
125 segmentation technique or anotherthat is most appropriate to analyze a given dataset is user dependent. To our
126 knowledge, no single segmentation technique can be generalized and universally used independently of the nature of
127 the samples. In the present study, we have chosen a simple segmentation technique by applying a threshold to the
128 gray scale images to separate the void space from the solid. This technique has been used in many studies in the last
129 two decades since the 2000's to characterize porosity in rocks, including some very and was applied in recent
130 studies in rock physics (Macente et al., 2019; Renard et al., 2019). The variability on tThe segmented porosity
131 volume depends strongly on the choice of the threshold and some studies have reporteddemonstrated that the final
132 porosity estimated by different segmentation methods couldcan vary within an error ofby 20% (Andrä et al., 2013).
133 A recent study has shown that, However, when the level of noise in the data is low, the differences in porosities
134 estimated between variousby different segmentation techniques is negligible (Figure 3h in Andrew, 2018). Our
135 data have beenwere acquired at a synchrotron where the parallel beam and high photon flux ensured a low level of
136 the noise in the images. In addition, theapplication of a non-local-means filter applied to our data has reduced the
137 noise level. For these reasons, we consider that theit was robust to apply choice of a simple thresholding technique is
138 robust for to this dataset andbut acknowledge that the porosity values we giveestimate later could have a small error
139 that cannot be estimated becausediffer by <20% from the ground truththe 'true' porosity of the rock is not known, as
140 discussed in(cf. Andrä et al., 2013; Hapca et al., 2013).

141 However, our segmentation procedurethis threshold range also captured cracks within a sample, which are likely to
142 result from depressurization during core recovery (Fig. 2b, Supplementary material 1: Fig. 1). To omit the cracks,
143 we utilized the morphological operation 'connected components' available in the software Avizo 9.1, which allows
144 volumes larger than selected number of connected voxels to be excluded from the binary label images. To each
145 sample we applied upper limits of 20 (43.94 μm^3), 50 (109.85 μm^3), 100 (219.7 μm^3) and 200 (439.4 μm^3) face
146 connected voxels. Total porosities estimates based on these operations are presented as percentages of the sample
147 volume in Supplementary material 1: Table 1. Unfortunately, this methodology results in either loss of larger pores
148 or inclusion of small cracks depending on the implemented limit of connected components, and thus the calculated
149 porosities include significant bias. Therefore, the operation 'connected components' was used only for visualization
150 purposes, and clusters of 200 face connected voxels were created to show the 3D volumes of segmented pore spaces
151 (Fig. 2c).

152 To omit the cracks, thresholded components with volumes larger than the volume of 200 connected voxels (439.4
153 μm^3) were excluded from the binary label images by using the morphological operation 'connected components'
154 built available in the software Avizo 9.1. Clusters of connected components were then created to visualize 3D
155 volumes of segmented pore spaces (Fig. 2c).

156 Unfortunately, this methodology results in either loss of larger pores or inclusion of small cracks depending on the
157 implemented limit of connected components, and thus calculating totalcalculated porosities includes significant bias.
158 InsteadInstead, the volumes and shape characteristics of segmented materials (including cracks i.e. without any data
159 limitation) were exported from Avizo software in numerical format, and volume distributions within a sample were
160 plotted on a logarithmic scale in Matlab (Fig. 3). Data up to a specific volume size were fit to a polynomial curve,
161 and then the curve was extrapolated to the X_axis intercept, which is the expected maximum pore size (Fig. 3). For
162 each sample the tTotal porositiesy wereas then estimated by integrating the curve, which excludes all volumes on
163 the right side of the curve. Total porosities are presented as a percentage of the whole sample volume (Fig. 3). The
164 implemented equations are presentedgiven in Supplementary material 1.

165

166 Pore shapes were analyzed on bivariate histograms plotted on Matlab by using the numerical pore characteristics,
167 previously extracted from Avizo software. Only pore volumes between 21.97 μm^3 (10 voxels) and 878.8 μm^3 (400
168 voxels) were included to avoid bias in the data due to insufficient voxel count and presence of cracks, respectively.

169 Individual pores in our dataset are separated (Fig. 2c). For each pore, the covariance matrix of the volume of each pore
170 was calculated, and the three eigenvalues of this covariance matrix were extracted. These three values correspond to
171 the three main orthogonal directions in each pore (i.e. the longest, medium and shortest axes) and we use them as
172 proxies to describe pore geometry. Thus, their amplitudes provide information on the spatial extension of the a given
173 pore and its shape. The ratio between the medium and largest eigenvalues of each pore defines its elongation (Fig.
174 4), the ratio between the smallest to and the largest eigenvalues defines its sphericity (Fig. 5), and the ratio of the
175 smallest to and the medium eigenvalues defines its flatness (Fig. 6).

176 The angles θ and ϕ that describe the orientation of the longest eigenvalue (i.e. axis) of each pore with respect to the
177 main global orthogonal axis system of the 3D scan were calculated. These angles were translated into trend and
178 plunge and then plotted on a lower hemisphere equal area stereographic projection with a probability density
179 contour to display the distribution of pore unit orientations (Fig. 7).

180 **3.4 Scanning electron microscopy (SEM)**

181 SEM images were collected on Zeiss Sigma-FF-SEM at the University of Otago's Centre for Electron Microscopy.
182 The SEM was operated at a working distance of 8.5 mm, an accelerating voltage of 10 keV and a 120 μm aperture
183 with dwell time of 100 μs . EDS maps were created by using Aztec Software (<https://www.oxford-instruments.com/products/microanalysis/energy-dispersive-x-ray-systems-eds-edx/eds-for-sem/eds-software-aztec>).
184

186 **3.5 Transmission electron microscopy (TEM)**

187 High resolution TEM images were collected on a FEI Tecnai G2 F20 X-Twin transmission electron microscope,
188 located at the German Research Centre for Geosciences (GFZ), Potsdam, Germany (Fig. 8Fig. 9). The instrument is
189 equipped with field-emission gun (FEG) electron source and high-angle annular dark-field (HAADF) Detector.
190 Images were collected from samples placed on a Gatan double-tilt holder at an accelerating voltage of 200kV. These
191 TEM samples were preparation was performed with focused ion beam (FIB) milling at GFZ Potsdam using a
192 HELIOS system operated at an accelerating voltage of 30 kV.

193 **34 Results**

194 **4.1 XCT-derived characteristics of porosity**

195 All samples contain low total porosities, ranging from 0.1% to 0.24% (Fig. 3). If different segmentation techniques
196 were applied, a variability between in the range that Andrew (2018) demonstrated is reasonable, from nearly nearly
197 0% to (e.g. Figure 3h in Andrew, 2018) to 20%, (Andrä et al., 2013) would correspond to porosities between 0.08%
198 and 0.29% in our samples. However, it should can be noted that the lower cataclasite sample (DFDP-1B 69_2.57)
199 has twice as much pore space (Fig. 3d) as any of the other samples. The characterized pore size volume distributions
200 range over almost three orders of magnitude for all samples (Fig. 3). Furthermore, the expected maximum pore size
201 volume was estimated to be largest in the PSZ-2 sample (DFDP-1B 69_2.54), reaching 862 μm^3 (Fig. 3c). All pores
202 are disconnected to each others.

203 In all samples, shape analyses of pores with volumes between 21.97 μm^3 (10 voxels) and 878.8 μm^3 (400 voxels)
204 demonstrate predominantly elongated (Fig. 4), non-spherical (Fig. 5) and flat pore shapes (Fig. 6). This is
205 particularly pronounced for the smaller pore volumes. The number of elongated pores per sample is
206 increasing increases in the upper foliated cataclasites (Fig. 4a and b) with increasing proximity to PSZ-2, where most
207 elongated pores occur (Fig. 4c). Conversely, the lower cataclasite sample demonstrates proportionally fewer
208 elongated pores within the sample (Fig. 4d). The degree of sphericity is uniform for all samples, and pores appear as
209 mainly non-spherical (Fig. 5). Few isolated spherical pores are manifested only by small pore volumes (Fig. 5). A

210 trend of increasing the number of flat pores is observed with increasing sample depth (Fig. 6), and most flat pores
211 are detected in the lower cataclasite (Fig. 6d).

212 The orientations of the individual pore units show two distinctive peaks with opposite vergence, defining bipolar
213 distributions of pore orientations (Fig. 7). The observed bipolarity is subtle in samples DFDP-1B 58_1.9 (Fig. 7a)
214 and DFDP-1B 69_2.48 (Fig. 7b), and more obvious in samples DFDP-1B 69_2.54 (Fig. 7c) and DFDP-1B 69_2.57
215 (Fig. 7d).

216 4.2 Microstructural characteristics of porosity

217 To demonstrate the microstructural arrangement of the cataclasites, we show representative SEM images from
218 sample DFDP-1B 69_248 (Fig. 8), previously described as a 'lower foliated cataclasite' by Toy et al., 2015. SEM
219 images presented here reveal rounded to sub-rounded crystalline clasts up to 100 µm in diameter (Fig. 8a, b), which
220 consist of ~50 % plagioclase, ~40 % K-feldspar, and ~10 % quartz and are elongated at angles of 0-30° to the
221 foliation. The surrounding matrix material is composed of finer grains (< 30 µm in diameter) of white micas,
222 chlorite, K-feldspar, calcite and Ti-oxide (Fig. 8c). Numerous quartz clasts contain microfractures, filled by calcite
223 and/or chlorite.

224 TEM characterization of the gouge material from PSZ-2 (sample DFDP-1B 69_2.54) reveals that the Alpine Fault
225 ~~gouges have composition, are composed of comprising~~ angular quartz and/or feldspar fragments (~200 nm in size),
226 wrapped by smaller phyllosilicates (< 100 nm long). This random fabric is ornamented by nanoscale pores (< 50
227 nm), distributed along all grain and phase boundaries, but especially abundant along within/around clay minerals
228 (Fig. 8Fig. 9a).

229 The gouge material also demonstrates phyllosilicate-rich areas, defined by an increase in the clay/clast ratio. In these
230 zones, fine (< 100 nm long) and coarser (few µm long) clay grains coexist and are aligned in wavy fabric that
231 surrounds sporadic protolith fragments (Fig. 8Fig. 9b). Pore spaces are again distributed along the boundaries of the
232 constituent mineral grains but some of them are larger (~0.5 µm) with and thin ellipsoidal or elongated shapes (Fig.
233 8Fig. 9b, c). These pores are commonly associated with inter-clay layer porosity. Large size pores are also observed
234 along quartz-feldspar grainphase boundaries. These latter, where pores are associated with multiple grains and
235 occasionally disrupt grain the boundaries, thus were labelled asas cracks along boundaries of quartz and/or feldspar
236 grains (i.e. fracture porosity) (Fig. 8Fig. 9d).

237 5 Discussion

238 5.1 Characteristics of porosity within the Alpine Fault core

239 Porosity analyses of samples from, or in close proximity to the two PSZs encountered in the DFDP-1B drill core
240 reveal total pore volumes between ~~—0.1%~~ and 0.24% (Fig. 3). These values are significantly lower than the porosity
241 estimates from other active faults in the world, such as: 0.2 to 5.7% total porosity in the core of the Nojima Fault,
242 Japan (Surma et al., 2003) and 0 to 18% in the San Andreas Fault core (Blackburn et al., 2009). The Alpine Fault
243 core contains total pore space volumes, comparable only with the lower porosities in these previous studies. It
244 should be noted that the smallest pore spaces captured in the XCT datasets are 1.3 µm in size due to resolution
245 acquisition constraints, whereas nanoscale porosity was identified on the TEM images. Therefore, the estimated total
246 porosities from XCT data represent only minimum values of the open pore spaces in the Alpine Fault core.
247 However, the addition of nanoscale porosity volumes is unlikely to dramatically affect the final total porosity of
248 these rocks because they comprise a very small total volume.

249

250 TEM images presented here mainly focus on nano-scale materials (Fig. 8Fig. 9a, c, d) but were also used to describe
251 the distribution of micro-porosity in these rocks (Figure 8Figure 9b). The pores visible on grain and phase
252 boundaries in~~On~~ figure 8~~figure 9b~~ pores have similar sizes comparable to the small range of pores segmented on
253 XCT images ($> 1.3 \mu\text{m}$ in diameter), and thus we conclude that this is the typical habit of both nano- and micro-
254 pores within the Alpine Fault core are distributed on grain and phase boundaries, especially of clay minerals (Fig.
255 ~~8~~Fig. 9). In addition, both quantitative micro-porosity shape analyses (Fig. 4, 5 and 6) and nano-pores identified on
256 TEM images (Fig. 8Fig. 9) reveal that a significant population of pores are predominantly non-spherical with
257 elongated, flat shapes. We attribute this observation to the tendency of these pores to ornament clay minerals where
258 pores are attained-distributed and elongated along their (001) planes (Fig. 8Fig. 9b, c and d).

259 Foliation in the upper cataclasites is defined by clay-sized phyllosilicates, that become more abundant with
260 proximity to the PSZ (Toy et al., 2015), where a weak clay fabric is developed (Schleicher et al., 2015). This gradual
261 enrichment in clay minerals coincides with the subtle development of bipolar distributions of pore orientations with
262 increasing sample depth (Fig. 7). This observation and the fact that pores are mainly attained-distributed along grain
263 boundaries of clays (Fig. 8Fig. 9) suggest that the distribution of clay minerals also controls pore orientations within
264 the Alpine Fault core. Previously, the phyllosilicate foliation in the Alpine Fault cataclasites has been used to define
265 shear direction (Toy et al., 2015). Thus, we speculate that pore orientations in these rocks are also systematically
266 related to the kinematic framework of the shear zone. If these pores represent remnants of fluid channels, their
267 spatial orientation is likely to reflect the fluid flow directions during deformation. To address this possibility more
268 data for systematic analyses of pore orientations are needed.

269 5.2 Porosity reduction within the Alpine Fault core

270 The comparatively lower porosity estimates of the Alpine Fault core than other active faults (e.g. the Nojima Fault,
271 Surma et al., 2003, and the San Andreas Fault, Blackburn et al., 2009) could~~be~~ be attributed to the fact that the
272 Alpine Fault is late in its c. 300 year seismic cycle and the last seismic event occurred in 1717– (Cochran et al.,
273 2017). Thus, ~~W~~we propose that the fault has almost completely sealed. Porosity of the fault cores is considered
274 widely thought~~believed~~ to evolve during the seismic cycle, when~~since~~ fault rupture can cause porosity porosities to
275 increase up to 10% (Marone et al., 1990), and the conse~~sub~~sequent healing by various mechanisms, (such as
276 mechanical compaction of the fault gouge and/or elimination of pore spaces within the fault core due to pressure
277 solution processes), lead~~cause~~sto porosity to decrease over time due to mechanical compaction of the fault gouge
278 and/or elimination of pore spaces within the fault core due to pressure solution processes (Sibson, 1990; Renard et
279 al., 2000; Faulkner et al., 2010). SEM TEM data presented here show that fine-grained chlorite and muscovite
280 grains are~~formed~~ as a cement in the cataclastic matrix (Fig. 8c). Our TEM data reveals the abundance of newly
281 precipitated authigenic clays, wrapped around coarser clay minerals (Fig. 8Fig. 9b). Furthermore, delicate clay
282 minerals form fringe structures (Fig. 8Fig. 9a), and strain shadows (Fig. 8Fig. 9c) around larger quartz-feldspar
283 grains. These microstructural observations demonstrate that pressure solution processes operated within these rocks
284 (Toy et al., 2015).

285 Evidence for pressure solution processes has been previously documented in all units, comprising the Alpine Fault
286 core (Toy et al., 2015). Abundant precipitation of alteration minerals (Sutherland et al., 2012), calcite filled
287 intragranular and cross-cutting veins (Williams et al., 2017), and the occurrence of newly formed smectite clays
288 (Schleicher et al., 2015) indicate extensive fluid-rock reactions. In addition, anastomosing networks of opaque
289 minerals (such as graphite; Kirilova et al., 2017), which define foliation in the upper cataclasites (Toy et al., 2015),
290 have been interpreted to be concentrated by pressure solution processes during aseismic creep (Toy et al., 2015;
291 Gratier et al., 2011). The petrological characteristics of the Alpine Fault core lithologies identify~~indicate~~ that
292 solution transfer mechanisms likely~~w~~as~~re~~likely the dominant mechanism for pore closure within these rocks.

293 Porosity estimates presented here are so low that presumably negligible variations in between samples can represent
294 significant gradients in porosity. For example, the increase of total porosity in sample DFDP-1B 69-2.57 with only
295 0.14%, manifests as twice as many open pore spaces in comparison to the rest of the analyzed samples (Fig. 3). In

296 addition, this is the only footwall sample analyzed here and as aforementioned already mentioned in section 3.1 does
297 not contain any gouge material. Post-rupture porosity reduction is known to operate three to four times faster within
298 fine-grained fault gouges than in coarser-grained cataclasites (Walder and Nur, 1984; Sleep and Blanpied, 1992;
299 Renard et al., 2000), which may explain the porosity differences demonstrated above, differences in total porosity
300 between the gouge containing samples and the footwall ultracataclasite – DFDP 1B-69 2.57 (Fig. 3). Furthermore,
301 previous studies documented less carbonate and phyllosilicate filling of cracks in the Alpine Fault footwall
302 cataclasites as compared to than in the hanging wall cataclasites (Sutherland et al., 2012; Toy et al., 2015),
303 suggesting more reactive fluids are present and isolated within the hanging wall of the Alpine Fault. Thus, more
304 intense dissolution-precipitation processes took place in the fault's hanging wall, which very likely resulted in more
305 efficient porosity reduction, as demonstrated by our porosity estimates (Fig. 3).

306 As aforementioned, porosity reduction is known to increase with time after an earthquake event due to post rupture
307 healing mechanisms (Sibson, 1990; Renard et al., 2000; Faulkner et al., 2010). Thus, the comparatively lower
308 porosity estimates of the Alpine Fault core than other active faults (e.g. the Nojima Fault, Surma et al., 2003, and the
309 San Andreas Fault, Blackburn et al., 2009) can be attributed to the fact that the Alpine Fault is late in its seismic
310 cycle (Cochran et al., 2017).

311 5.3 Effects of porosity on the Alpine Fault strength

312 The extremely Very low porosity estimates are presented here (Fig. 3). are consistent with the Very low
313 permeabilities of 10^{-18} m^2 were also measured experimentally in clay-rich cataclasites and gouges from the Alpine
314 Fault zone (Carpenter et al., 2014). In addition, the documented difference of total porosities between the hanging
315 wall and footwall samples (Fig. 3) implies may be interpreted as to reflect different intensities of pressure solution
316 processes, and thus compartmented compartmentalisation compartmentalization of percolating fluids propagation.
317 Our porosity data thus provide independent verification is comparable with of show a spatial trend similar to the
318 permeability measurements in that study of (Carpenter et al., (2014). This observation and yields increased
319 confidence in their the interpretation of (Carpenter et al. (2014)) of a permeability gradient with distance from the
320 PSZ, which itself acts as a hydraulic seal (Sutherland, et al., 2012). The existence of such a barrier to flow is
321 characteristic for faults undergoing creep and locked faults (Rice, 1992; Labaume et al., 1997; Wiersberg and
322 Erzinger, 2008). However, much higher permeabilities in the surrounding damaged rocks (Carpenter et al., 2014)
323 allow fast propagation of fluids within them and can cause localization of high fluid pressures on one side or the
324 other of a hydraulic seal (Sibson, 1990). Such fluid pressures can enhance gouge compaction and pressure solution
325 processes within the fault core, which will eventually introduce zones of weakness and thus may trigger fault slip
326 (Faulkner et al., 2010).

327 Previous studies and the observations presented here show that fluids were present in the Alpine Fault rocks. Fluid-
328 filled pores represent a favorable environment for mineral precipitation, which can affect the fault strength in two
329 ways: (i) Very small decrease of these critically low total porosities due to mineral precipitation would cause fluid
330 pressurization, which is a well-known fault weakening mechanism described by (Byerlee, (1990); and Sibson,
331 (1990)). However, this pressure increase will could be slightly offset by inclusion of fluids into new hydrous
332 minerals; (ii) deposition of frictionally weak phases (such as clay minerals and graphite), especially if they decorate
333 grain contacts and/or form interlinked weak layers, would lower the overall frictional strength (Rutter et al., 1976;
334 Niemeijer et al., 2010).

335 Precipitation of ed authigenic clay minerals was were identified on in our TEM data (Fig. 8Fig. 9) and also
336 documented by previous studies (Schleicher et al., 2015). As well as having low frictional strengths (Moore and
337 Lockner, 2004), clay minerals may also contribute to the formation of an impermeable seal if they form an aligned
338 fabric, and thus can which can enhance the likelihood of fluid-pressurization in the fault rocks (Rice, 1992; Faulkner
339 et al., 2010). In addition, graphite, which was previously documented in these rocks by previous studies (Kirilova et
340 al., 2017), may effectively weaken the fault due to mechanical smearing (Rutter et al., 2013) and/or localized

341 precipitation within strained areas (Upton and Craw, 2008). Such graphite precipitation within shear surfaces was
342 previously documented by Kirilova et al. (2017).

343 In summary, the presence of trapped fluids in the low porosity rocks of the Alpine Fault core possibly controls the
344 mechanical behavior of the fault and could be responsible for future rupture initiation due to fluid pressurization
345 and/or precipitation of weak mineral phases. This hypothesis is further supported by an experimental study showing
346 that the DFDP-1 gouges are frictionally strong in the absence of elevated fluid pressure (Boulton et al., 2014).

347 **6 Conclusions**

348 Analyses of XCT-datasets and TEM images of borehole samples from the core of the Alpine Fault reveal micro- and
349 nanoscale pores, distributed along grain boundaries of the constituent mineral phases, especially clay minerals. The
350 tendency of these pores to ornament clays defines their predominantly non-spherical, elongated, flat shapes and the
351 bipolar distribution of pore orientations. The documented extremely low total porosities (~~from in the range~~ 0.1 to
352 0.24 %) in these rocks suggest effective porosity reduction and fault healing. Microstructural observations presented
353 here and documented in previous studies indicate that pressure solution processes were the dominant healing
354 mechanism, and that fluids were present in these rocks. Therefore, fluid-filled pores may be places where ~~fluid~~
355 ~~ever pressures elevated pore fluid pressures~~ develop, due to further mineral precipitation that decreases the already
356 critically low total porosities. – Alternatively, ~~they these pores~~ may also facilitate the deposition of weak mineral
357 phases (such as clay minerals and graphite) that may very effectively weaken the fault. We conclude that the current
358 state of the fault core porosity is possibly a controlling factor on the mechanical behaviour of the Alpine Fault and
359 will likely play a key role in the initiation of the next fault rupture.

360 **Data availability.**

361 Avizo screenshots, total porosity estimates, Matlab ~~code scripts~~ and numerical data of pore volumes can be found in
362 Supplementary material 1.

363 **Authors contribution**

364 Kirilova reconstructed, processed, and analysed the XCT datasets presented here, interpreted the TEM data and
365 prepared the manuscript. Most of this work was performed during Kirilova's PhD under the academic guidance of
366 Toy. Toy and Gessner collected the XCT data with technical support by Xiao. Renard and Sauer contributed with
367 valuable discussion about XCT data analyses and edited the manuscript. Wirth enabled TEM data acquisition and
368 provided his expertise on TEM data interpretation. Matsu ~~sumura collected and analyzed the presented SEM data~~. The
369 final version of this manuscript benefits from collective intellectual input.

370 **Competing interests**

371 The authors declare that they have no conflict of interest.

372 **Acknowledgments**

373 We gratefully acknowledge funding from the Advances Photon Source (GUP 31177). This research used resources
374 of the Advanced Photon Source, a U.S. Department of Energy (DOE) Office of Science User Facility operated for
375 the DOE Office of Science by Argonne National Laboratory under Contract No. DE-AC02-06CH11357. Avizo
376 workstation was built at the University of Otago with financial support provided by Nvidia[®] Corporation[®], Royal
377 Society of New Zealand[®]'s Rutherford fellowships (16-UOO-001), the Ministry of Business and Innovation[®]'s
378 Endeavor Fund (C05X1605/GNS-MBIE00056), and a subcontract to the Tectonics and Structure of Zealandia
379 Program at GNS Science (GNS-DCF00020). Publishing bursary funding provided by the University of Otago is
380 greatly appreciated. We thank Sherry Mayo for helping with the reconstruction process of XCT data and Andrew

381 Squelch for providing use of the Avizo workstation, located at CSIRO, Perth, Australia during the initial data
382 analyses. Special thanks to Reed Debaets for assistance with the development of Matlab code. [Klaus Gessner](#)
383 [publishes with permission of the Executive Director, Geological Survey of Western Australia.](#)

384 **References**

385 [Andrä, H., Combaret, N., Dvorkin, J., Glatt, E., Han, J., Kabel, M., Keehmd, Y., Krzikallac, F., Leed, M.,](#)
386 [Madonnae, C., Marshb, M., Mukerjc, T., Saengere, E. H., Sainf, R., Saxenac, N., Rickera, S., Wiegmann, A., and](#)
387 [Zhanf, X., ... & Marsh, M., 2013, Digital rock physics benchmarks—Part I: Imaging and segmentation. Computers](#)
388 [& Geosciences, 50, 25-32.](#)

389 [Andrew, M., 2018, A quantified study of segmentation techniques on synthetic geological XRM and FIB-SEM](#)
390 [images, Computational Geosciences, 22\(6\), 1503-1512.](#)

391 Berryman, K. R., Cochran, U. A., Clark, K. J., Biasi, G. P., Langridge, R. M., and Villamor, P., 2012, Major
392 earthquakes occur regularly on an isolated plate boundary fault, *Science*, 336(6089), 1690-1693.

393 Blackburn, E. D., Hadizadeh, J., and Babaie, H. A., 2009, A microstructural study of SAFOD gouge from actively
394 creeping San Andreas Fault zone: Implications for shear localization models, *in* AGU Fall Meeting Abstracts.

395 Buades, A., Coll, B. and Morel, J. M., 2005, A non-local algorithm for image denoising, *in* Computer Vision and
396 Pattern Recognition, IEEE Computer Society Conference, Vol. 2, pp. 60-65.

397 Boulton, C., Carpenter, B. M., Toy, V., and Marone, C., 2012, Physical properties of surface outcrop cataclastic
398 fault rocks, Alpine Fault, New Zealand, *Geochemistry, Geophysics, Geosystems*, 13, Q01018,
399 doi:10.1029/2011GC003872.

400 Boulton, C., Moore, D. E., Lockner, D. A., Toy, V. G., Townend, J., and Sutherland, R., 2014, Frictional properties
401 of exhumed fault gouges in DFDP-1 cores, Alpine Fault, New Zealand, *Geophysical Research Letters*, 41(2), 356-
402 362.

403 Byerlee, J., 1990, Friction, overpressure and fault normal compression, *Geophysical Research Letters*, 17(12), 2109-
404 2112.

405 Carpenter, B. M., Kitajima, H., Sutherland, R., Townend, J., Toy, V. G., and Saffer, D. M., 2014, Hydraulic and
406 acoustic properties of the active Alpine Fault, New Zealand: Laboratory measurements on DFDP-1 drill core, *Earth*
407 and *Planetary Science Letters*, 390, 45-51.

408 Cochran, U. A., Clark, K. J., Howarth, J. D., Biasi, G. P., Langridge, R. M., Villamor, P., ...[Berryman, K. R.,](#) and
409 Vandergoes, M. J., 2017, A plate boundary earthquake record from a wetland adjacent to the Alpine fault in New
410 Zealand refines hazard estimates, *Earth and Planetary Science Letters*, 464, 175-188.

411 Faulkner, D. R., Jackson, C. A. L., Lunn, R. J., Schlische, R. W., Shipton, Z. K., Wibberley, C. A. J., and Withjack,
412 M. O., 2010, A review of recent developments concerning the structure, mechanics and fluid flow properties of fault
413 zones, *Journal of Structural Geology*, 32(11), 1557-1575.

414 Fusseis, F., Xiao, X., Schrank, C., and De Carlo, F., 2014, A brief guide to synchrotron radiation-based
415 microtomography in (structural) geology and rock mechanics, *Journal of Structural Geology*, 65, 1-16.

416 Girault, F., Adhikari, L. B., France-Lanord, C., Agrinier, P., Koirala, B. P., Bhattacharai, M., and Perrier, F., 2018,
417 Persistent CO₂ emissions and hydrothermal unrest following the 2015 earthquake in Nepal, *Nature*
418 *Communications*, 9(1), 2956.

419 Gratier, J.-P., Favreau, P., and Renard, F., 2003, Modelling fluid transfer along California faults when integrating
 420 pressure solution crack sealing and compaction processes, *Journal of Geophysical Research*, 108, 2104,
 421 doi:10.1029/2001JB000380, B2.

422 Gratier, J. P., 2011, Fault permeability and strength evolution related to fracturing and healing episodic processes
 423 (years to millennia): the role of pressure solution, *Oil and Gas Science and Technology–Revue d’IFP Energies
 424 nouvelles*, 66(3), 491-506.

425 Gratier, J. P., and Gueydan, F., 2007, Effect of Fracturing and Fluid–Rock Interaction on Seismic Cycles, *Tectonic
 426 Faults: Agents of Change on a Dynamic Earth*, 95, 319e356.

427 Gureyev, TE, Nesterets, Y, Ternovski, D, Wilkins, SW, Stevenson, AW, Sakellariou, A and Taylor, JA 2011,
 428 Toolbox for advanced x-ray image processing, in *Advances in Computational Methods for X-Ray Optics II* edited
 429 by M Sanchez del Rio and O Chubar, *Advances in Computational Methods for X-Ray Optics II*, San Diego, USA,
 430 21-25 August 2011: SPIE - The International Society of Optics and Photonics 8141.

431 [Iassonov, P., Gebrenegus, T., and Tuller, M., 2009, Segmentation of X-ray computed tomography images of porous
 432 materials: A crucial step for characterization and quantitative analysis of pore structures. *Water resources research*,
 433 45\(9\), W09415, doi:10.1029/2009WR008087.](#)

434 Janssen, C., Wirth, R., Reinicke, A., Rybacki, E., Naumann, R., Wenk, H. R., and Dresen, G., 2011, Nanoscale
 435 porosity in SAFOD core samples (San Andreas Fault), *Earth and Planetary Science Letters*, 301(1), 179-189.

436 [Hapca, S. M., Houston, A. N., Otten, W., and Baveye, P. C., 2013, New local thresholding method for soil images
 437 by minimizing grayscale intra-class variance, *Vadose Zone Journal*, 12\(3\), 12 \(3\): vzej2012.0172.](#)

438 Labaume, P., Maltman, A. J., Bolton, A., Tessier, D., Ogawa, Y., and Takizawa, S. 1997, Scaly fabrics in sheared
 439 clays from the décollement zone of the Barbados accretionary prism, in Shipley, T.H., Ogawa, Y., Blum, P., and
 440 Bahr, J.M. (Eds.), *Proceedings of the Ocean Drilling Program Scientific Results*, 59-78.

441 Kirilova, M., Toy, V. G., Timms, N., Halfpenny, A., Menzies, C., Craw, D., [Beyssac, O., Sutherland, R., Townend, J., Boulton, C., Carpenter, B., Cooper, A., Grieve, J., Little, T., Morales, L., Morgan, C., Mori, H., Sauer, K., Schleicher, A., Williams, J., and Craw, L... and Carpenter, B. M.](#), 2017, Textural changes of graphitic carbon by
 442 tectonic and hydrothermal processes in an active plate boundary fault zone, Alpine Fault, New Zealand, *Geological
 443 Society, London, Special Publications*, 453, SP453-13.

444 [Ma, X., Kittikunakorn, N., Sorman, B., Xi, H., Chen, A., Marsh, M., ... Mongeau, A., Piché, N., WilliamsIII, E. O., and Skomski, D., 2020, Application of Deep Learning Convolutional Neural Networks for Internal Tablet Defect
 445 Detection: High Accuracy, Throughput, and Adaptability, *Journal of Pharmaceutical Sciences*, 109\(4\), 1447-1457.](#)

446 [Macente, A., Vanorio, T., Miller, K. J., Fusseis, F., and Butler, I. B., 2019, Dynamic Evolution of Permeability in
 447 Response to Chemo-Mechanical Compaction, *Journal of Geophysical Research: Solid Earth*, 124\(11\), 11204-11217.](#)

448 Marone, C., Raleigh, C. B., and Scholz, C. H., 1990, Frictional behavior and constitutive modeling of simulated
 449 fault gouge, *Journal of Geophysical Research: Solid Earth*, 95(B5), 7007-7025.

450 Niemeijer, A., Marone, C., and Elsworth, D., 2010, Fabric induced weakness of tectonic faults, *Geophysical
 451 Research Letters*, 37, L03304, doi:10.1029/2009GL041689.

452 Norris, R. J., and Cooper, A. F., 1995, Origin of small-scale segmentation and transpressional thrusting along the
 453 Alpine fault, New Zealand. *Geological Society of America Bulletin*, 107(2), 231-240.

457 Norris, R. J., and Cooper, A. F., 2001, Late Quaternary slip rates and slip partitioning on the Alpine Fault, New
458 Zealand. *Journal of Structural Geology*, 23(2), 507-520.

459 Norris, R. J., and Toy, V. G., 2014, Continental transforms: A view from the Alpine Fault, *Journal of Structural
460 Geology*, 64, 3-31.

461 Renard, F., Gratier, J. P., and Jamtveit, B., 2000, Kinetics of crack-sealing, intergranular pressure solution, and
462 compaction around active faults, *Journal of Structural Geology*, 22(10), 1395-1407.

463 [Renard, F., McBeck, J., Cordonnier, B., Zheng, X., Kandula, N., Sanchez, J. R., Kobchenko, M., Noirlie, C., Zhu, W., Meakin, P., Fusseis, F., and Dag K. Dysthe, ... & Fusseis, F., 2019, Dynamic in situ three-dimensional imaging and digital volume correlation analysis to quantify strain localization and fracture coalescence in sandstone, Pure and Applied Geophysics, 176\(3\), 1083-1115.](#)

467 Rice, J. R., 1992, Fault stress states, pore pressure distributions, and the weakness of the San Andreas fault,
468 *International Geophysics*, 51, 475-503.

469 Rutter, E. H., and Elliott, D., 1976, The kinetics of rock deformation by pressure solution, *Philosophical
470 Transactions for the Royal Society of London, Series A, Mathematical and Physical Sciences*, 283, 203-219.

471 Rutter, E. H., Hackston, A. J., Yeatman, E., Brodie, K. H., Mecklenburgh, J., and May, S. E., 2013, Reduction of
472 friction on geological faults by weak-phase smearing, *Journal of Structural Geology*, 51, 52-60.

473 Schleicher, A. M., Sutherland, R., Townend, J., Toy, V. G., and Van Der Pluijm, B. A., 2015, Clay mineral
474 formation and fabric development in the DFDP-1B borehole, central Alpine Fault, New Zealand, *New Zealand
475 Journal of Geology and Geophysics*, 58(1), 13-21.

476 Schuck, B., Schleicher, A. M., Janssen, C., Toy, V. G., and Dresen, G., 2020, Fault zone architecture of a large
477 plate-bounding strike-slip fault: a case study from the Alpine Fault, New Zealand. *Solid Earth*, 11(1), 95-124.

478 Secor, D. T., 1965, Role of fluid pressure in jointing, *American Journal of Science*, 263(8), 633-646.

479 Sibson, R. H., 1990, Conditions for fault-valve behaviour, *Geological Society, London, Special Publications*, 54(1),
480 15-28.

481 Sleep, N. H., and Blanpied, M. L., 1992, Creep, compaction and the weak rheology of major faults, *Nature*,
482 359(6397), 687-692.

483 Surma, F., Géraud, Y., and Pezard, P., 2003, Porosity network of the Nojima fault zone in the Hirabayashi hole
484 (Japan), in *EGS-AGU-EUG Joint Assembly*.

485 Sutherland, R., Eberhart-Phillips, D., Harris, R. A., Stern, T., Beavan, J., Ellis, S. Henrys, S., Cox, S., Norris, R.J.,
486 Berryman, K.R. and Townend, J., 2007, Do great earthquakes occur on the Alpine fault in central South Island, New
487 Zealand?, In: *A continental plate boundary: tectonics at South Island, New Zealand, Geophysical Monograph*,
488 American Geophysical Union, 235-251.

489 Sutherland, R., Toy, V. G., Townend, J., Cox, S. C., Eccles, J. D., Faulkner, D. R Prior, D.J., Norris, R.J., Mariani,
490 E., Boulton, C. and Carpenter, B.M., 2012, Drilling reveals fluid control on architecture and rupture of the Alpine
491 fault, New Zealand, *Geology*, 40(12), 1143-1146.

492 Sutherland, R., Townend, J., Toy, V., Upton, P., Coussens, J., Allen, M., and Boles, A., 2017, Extreme
493 hydrothermal conditions at an active plate-bounding fault, *Nature*, 546, 137-140, doi: 10.1038/nature22355.

494 Toy, V. G., Boulton, C. J., Sutherland, R., Townend, J., Norris, R. J., Little, T. A., and Scott, H., 2015, Fault rock
495 lithologies and architecture of the central Alpine fault, New Zealand, revealed by DFDP-1 drilling, *Lithosphere*,
496 L395-1.

497 Toy, V. G., Sutherland, R., Townend, J., Allen, M., Becroft, L., Boles, A., Boulton, C., Carpenter, B., Cooper, A.,
498 Cox, S., Daube, C., Faulkner, D., Halfpenny, A., Kato, N., Keys, S., Kirilova, M., Kometani, Y., Little, T., Mariani,
499 E., Melosh, B., Menzies, C., Morales, L., Morgan, C., Mori, C., Niemeijer, A., ... and Zimmer, M., 2017, Bedrock
500 Geology of DFDP-2B, Central Alpine Fault, New Zealand, *New Zealand Journal of Geology and Geophysics*,
501 60(4), 497-518.

502 Upton P. and Craw D., 2008, Modelling the role of graphite in development of a mineralised mid-crustal shear zone,
503 Macraes mine, New Zealand, *Earth and Planetary Science Letters* 266: 245-255.

504 Walder, J., and Nur, A., 1984, Porosity reduction and crustal pore pressure development, *Journal of Geophysical*
505 *Research: Solid Earth*, 89(B13), 11539-11548.

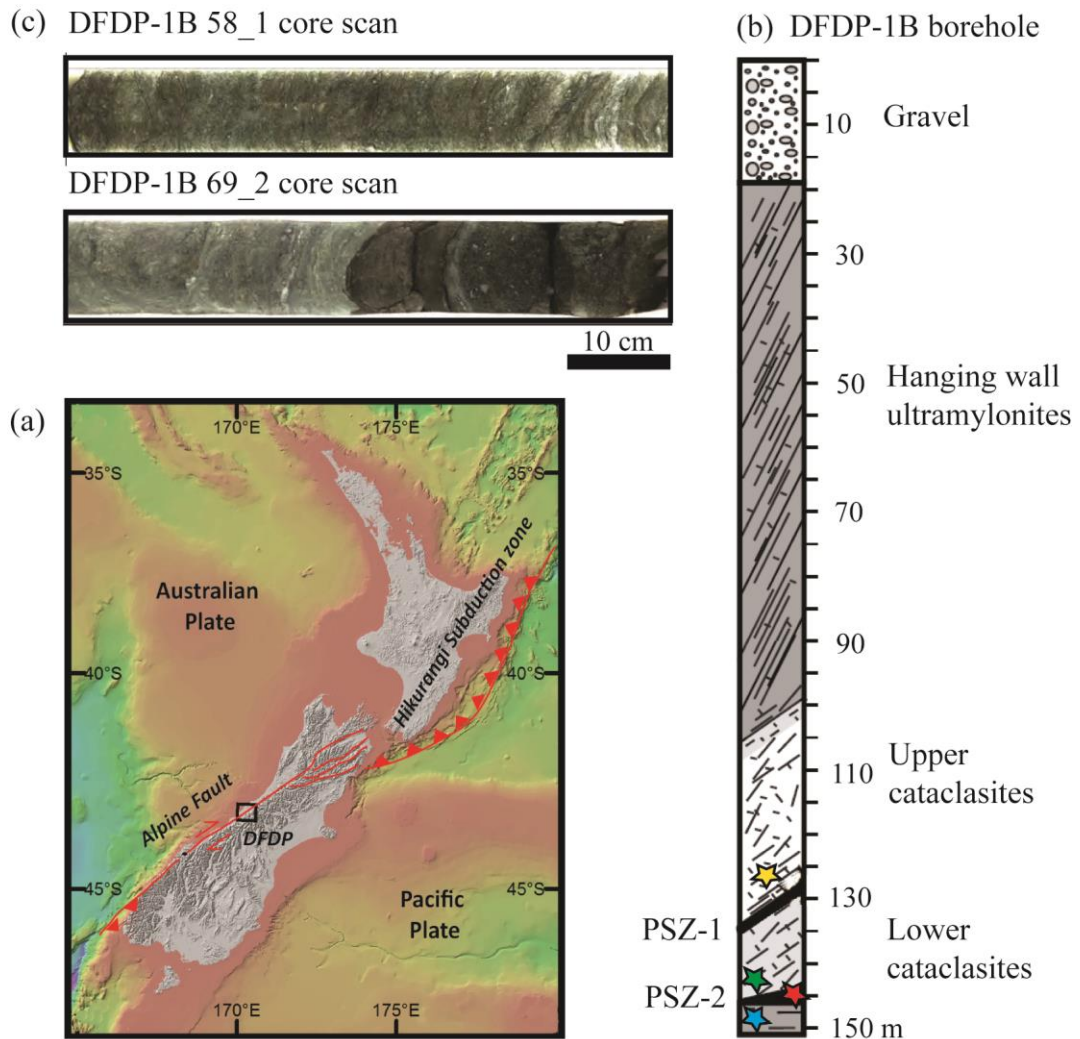
506 Walsh, J. B., 1965, The effect of cracks on the uniaxial elastic compression of rocks, *Journal of Geophysical*
507 *Research*, 70(2), 399-411.

508 Wiersberg, T. and Erzinger, J., 2008, Origin and spatial distribution of gas at seismogenic depths of the San Andreas
509 Fault from drill-mud gas analysis: *Applied Geochemistry*, v. 23, no. 6, p. 1675-1690.

510 Williams, J. N., Toy, V. G., Smith, S. A. and Boulton, C., 2017, Fracturing, fluid-rock interaction and mineralisation
511 during the seismic cycle along the Alpine Fault, *Journal of Structural Geology*, 103, 151-166.

512 [Zhu, W., Allison, K. L., Dunham, E. M., Yang, Y., 2020, Fault valving and pore pressure evolution in simulations of](#)
513 [earthquake sequences and aseismic slip, Nature Communications, 11, 4833, doi.org/10.1038/s41467-020-18598-z.](#)

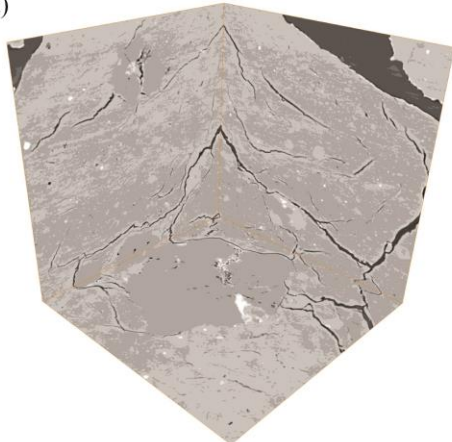
514



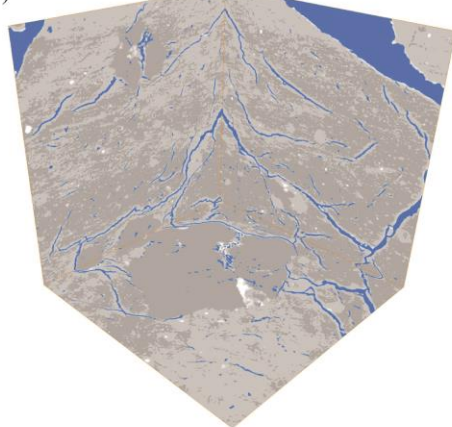
517 **Figure 1.** (a) Location map of DFDP drill sites (a bathymetric map compiled by NIWA). [Drill site coordinates: 43°17'5"S, 170°24'22"E](#) (b) Schematic diagram of the sampled lithologies in DFDP-1B borehole (modified after
 518 Sutherland et al., 2012). (c) Scans of DFDP-1B drill core. Samples were collected from the locations indicated with
 519 stars: yellow – DFDP-1B 58_1.9; green – DFDP-1B 69_2.48; red – DFDP-1B 69_2.54; blue – DFDP-1B 69_2.57.
 520

DFDP - 1B 69-2.57

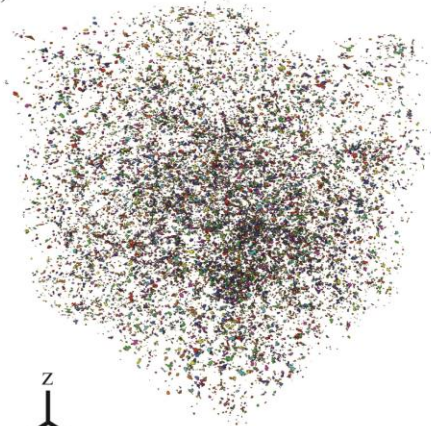
(a)



(b)



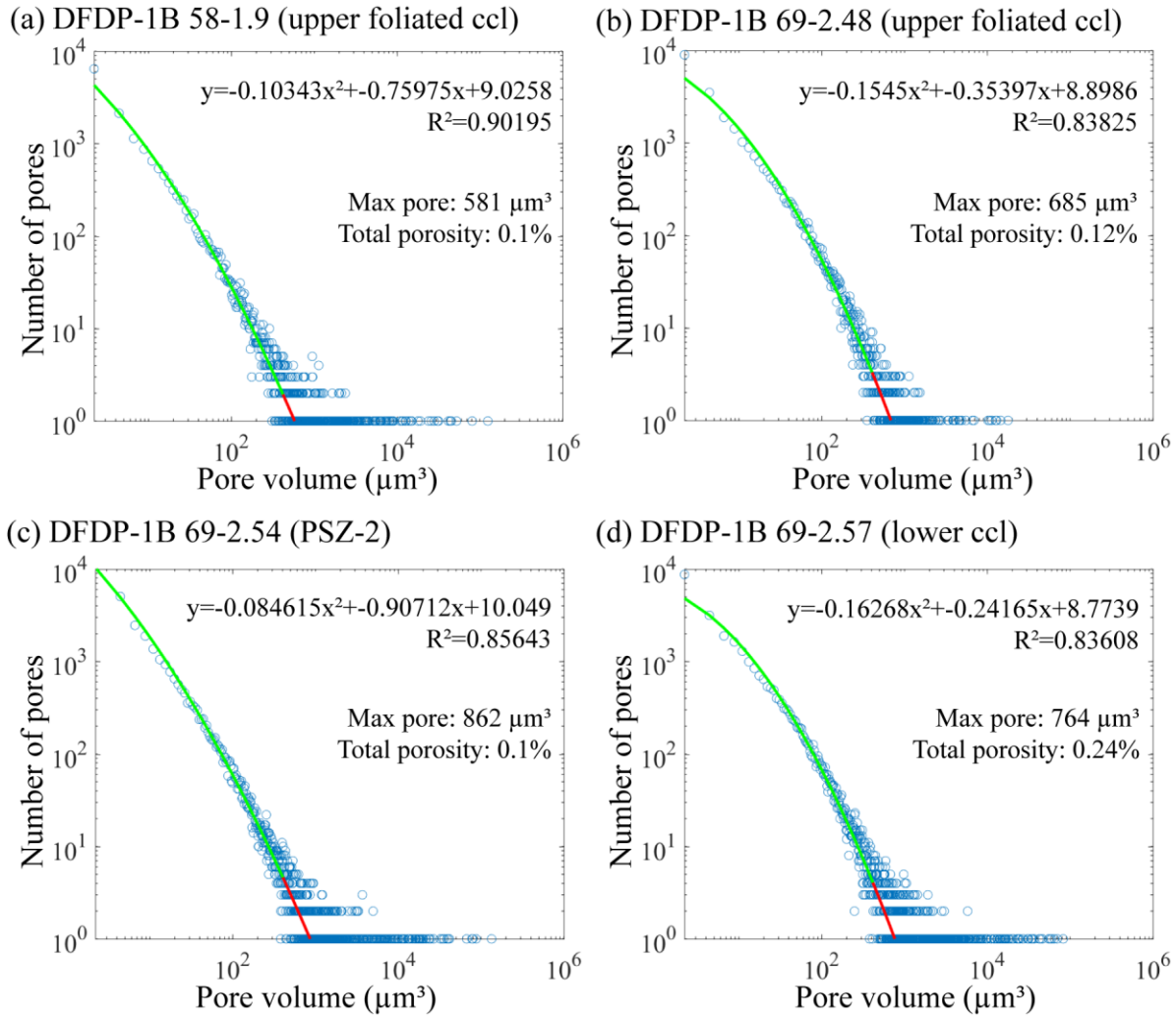
(c)



521
y
z
x

521

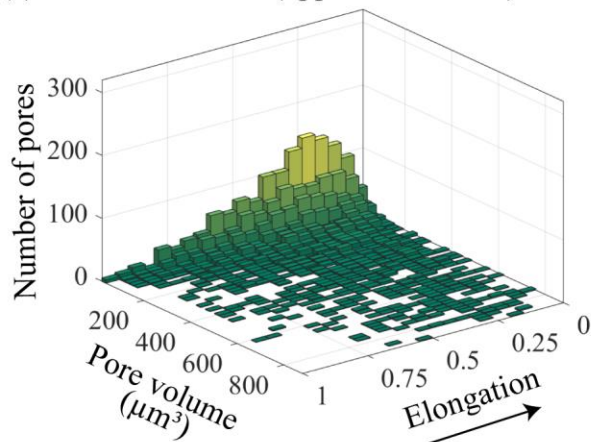
522 **Figure 2.** X-ray tomography data processing workflow. (a) Gray scale images in xy, xz and yz directions (b)
523 Threshold of the darkest gray scale phase in each sample, corresponding to voids (pores and fractures); (c) 3D
524 volume of the segmented pore spaces after removal of the fractures due to sample decompaction and coring
525 damaging effects were removed.



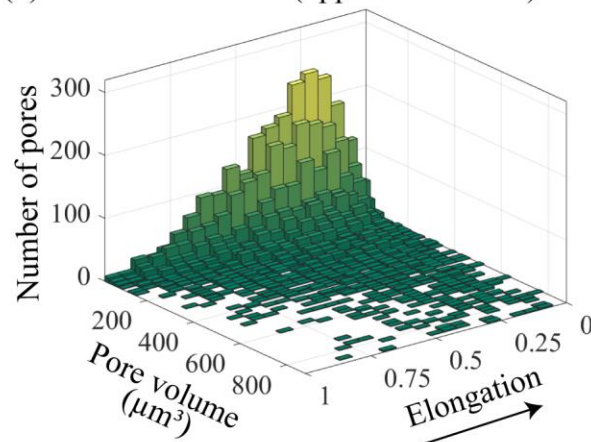
526

527 **Figure 3.** Plots of pore volume versus number of pores for each sample. Estimates of total porosity and size of the
528 maximum expected pore are also shown, as well as the curve fitting function for each dataset.

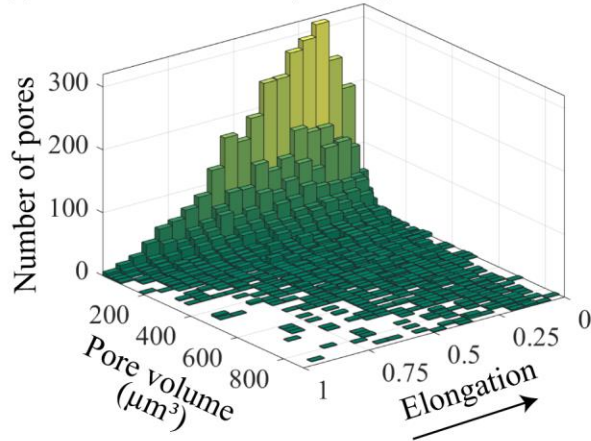
529 (a) DFDP-1B 58-1.9 (upper foliated ccl)



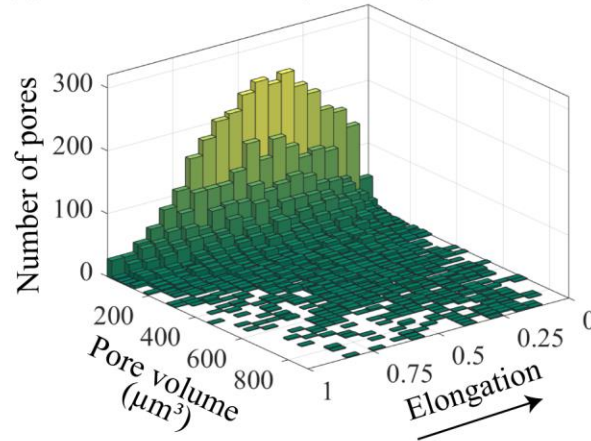
530 (b) DFDP-1B 69-2.48 (upper foliated ccl)



531 (c) DFDP-1B 69-2.54 (PSZ-2)



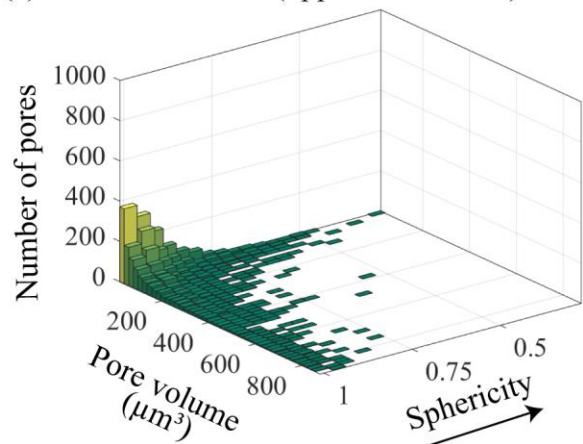
532 (d) DFDP-1B 69-2.57 (lower ccl)



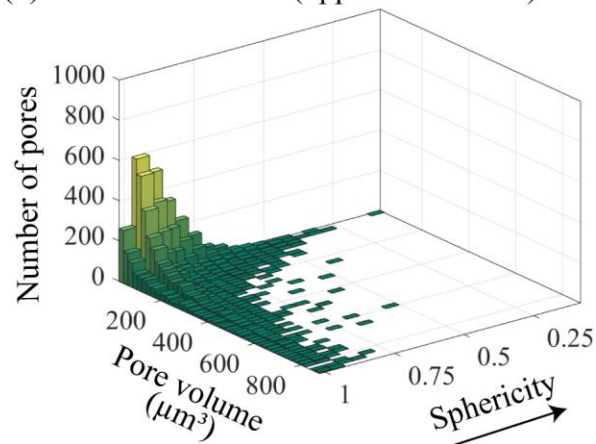
529

530 **Figure 4.** Bivariate histograms showing elongation versus pore volume (μm^3) and number of pores for each sample.
531 The arrow indicates the direction of increasing elongation. [Here, the elongation is defined as the ratio between the](#)
532 [medium and the largest eigenvalues \(i.e. axis\) of each pore.](#)

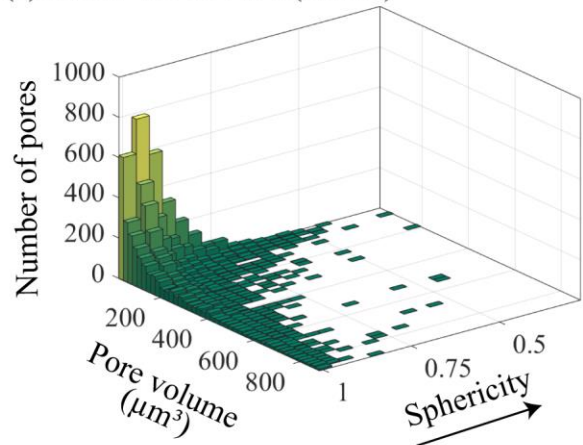
533 (a) DFDP-1B 58-1.9 (upper foliated ccl)



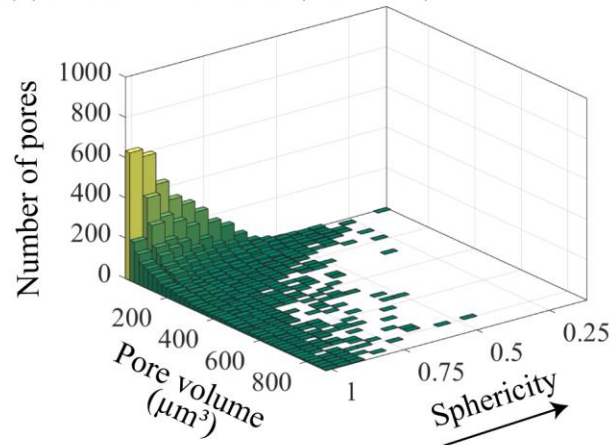
535 (b) DFDP-1B 69-2.48 (upper foliated ccl)



533 (c) DFDP-1B 69-2.54 (PSZ-2)



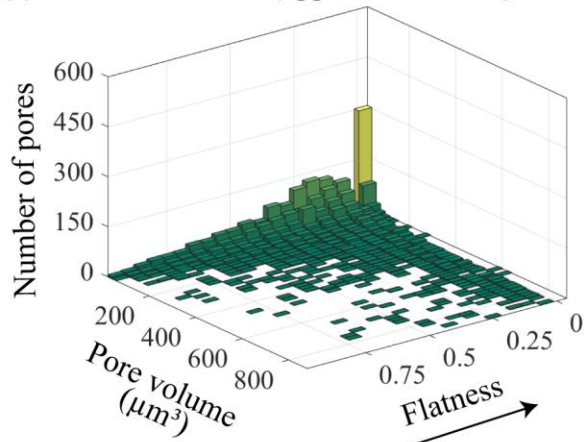
535 (d) DFDP-1B 69-2.57 (lower ccl)



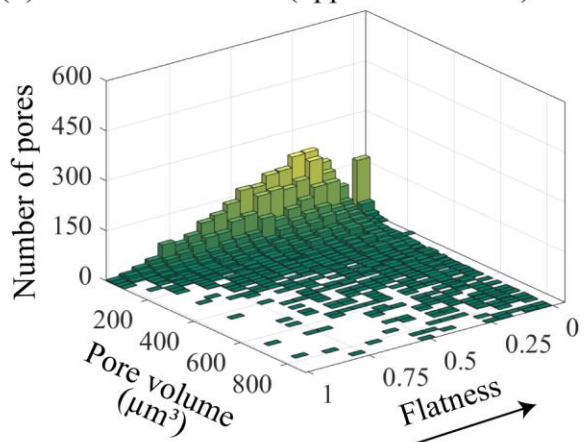
533

534 **Figure 5.** Bivariate histograms showing sphericity versus pore volume (μm^3) and number of pores for each sample.
535 The arrow indicates the direction of increasing sphericity. [Here, the sphericity is defined as the ratio between the](#)
536 [smallest and the largest eigenvalues \(i.e. axis\) of each pore.](#)

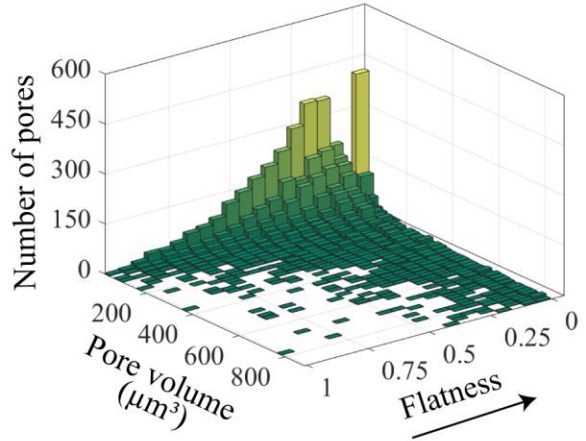
537 (a) DFDP-1B 58-1.9 (upper foliated ccl)



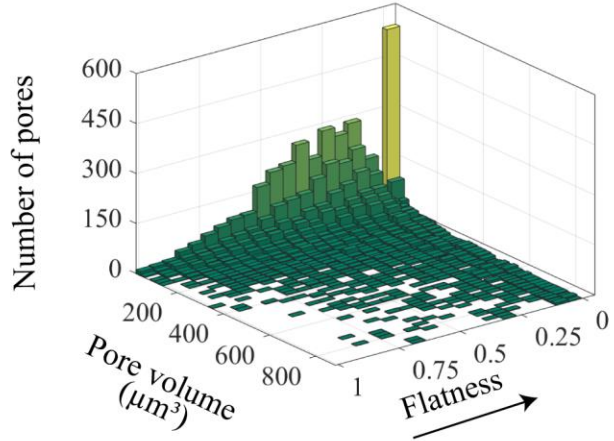
539 (b) DFDP-1B 69-2.48 (upper foliated ccl)



537 (c) DFDP-1B 69-2.54 (PSZ-2)



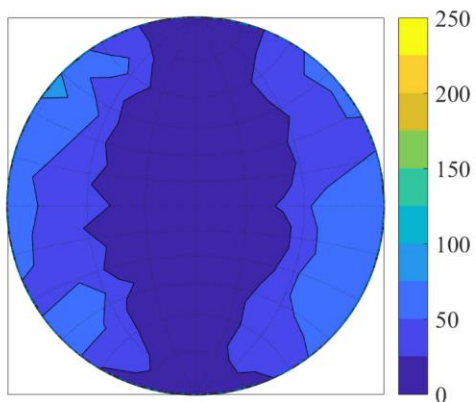
539 (d) DFDP-1B 69-2.57 (lower ccl)



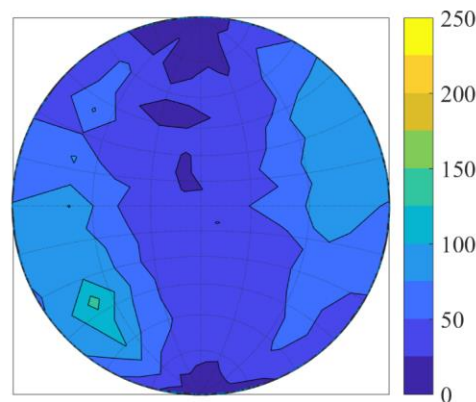
537

538 **Figure 6.** Bivariate histograms showing flatness versus pore volume (μm^3) and number of pores for each sample.
539 The arrow indicates the direction of increasing flatness. [Here, the flatness is defined as the ratio of the smallest and](#)
540 [the medium eigenvalues \(i.e. axis\) of each pore.](#)

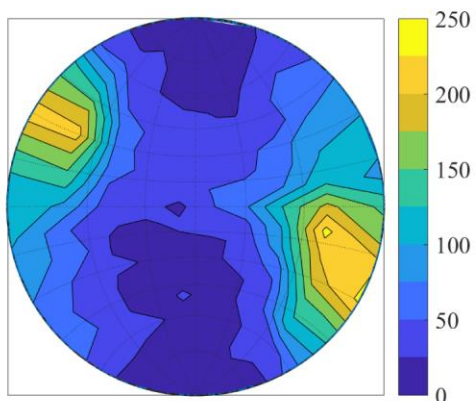
541 (a) DFDP-1B 58-1.9 (upper foliated ccl)



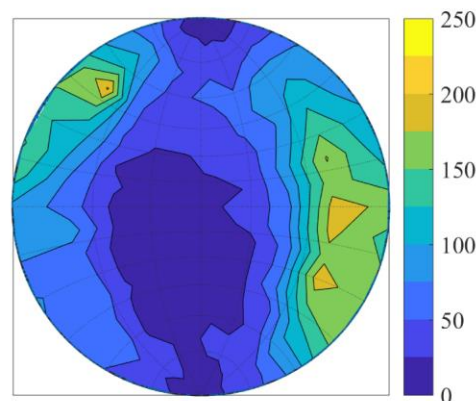
542 (b) DFDP-1B 69-2.48 (upper foliated ccl)



543 (c) DFDP-1B 69-2.54 (PSZ-2)

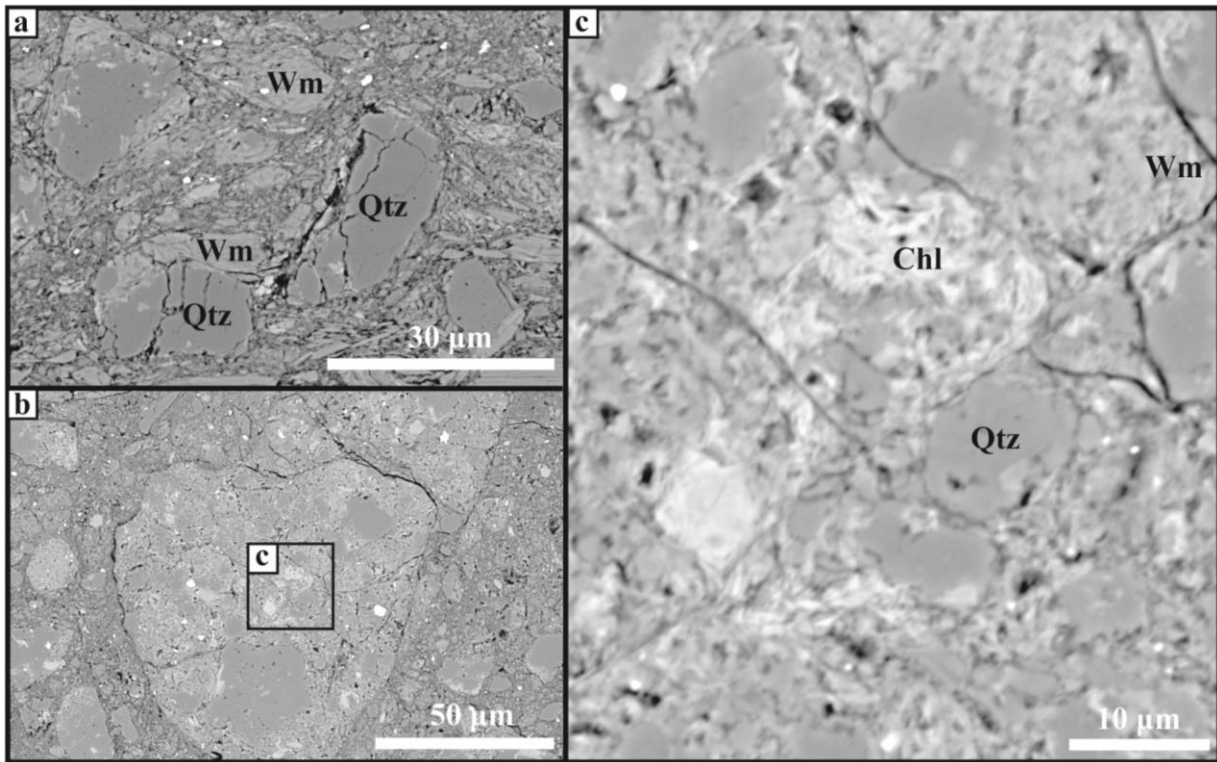


544 (d) DFDP-1B 69-2.57 (lower ccl)



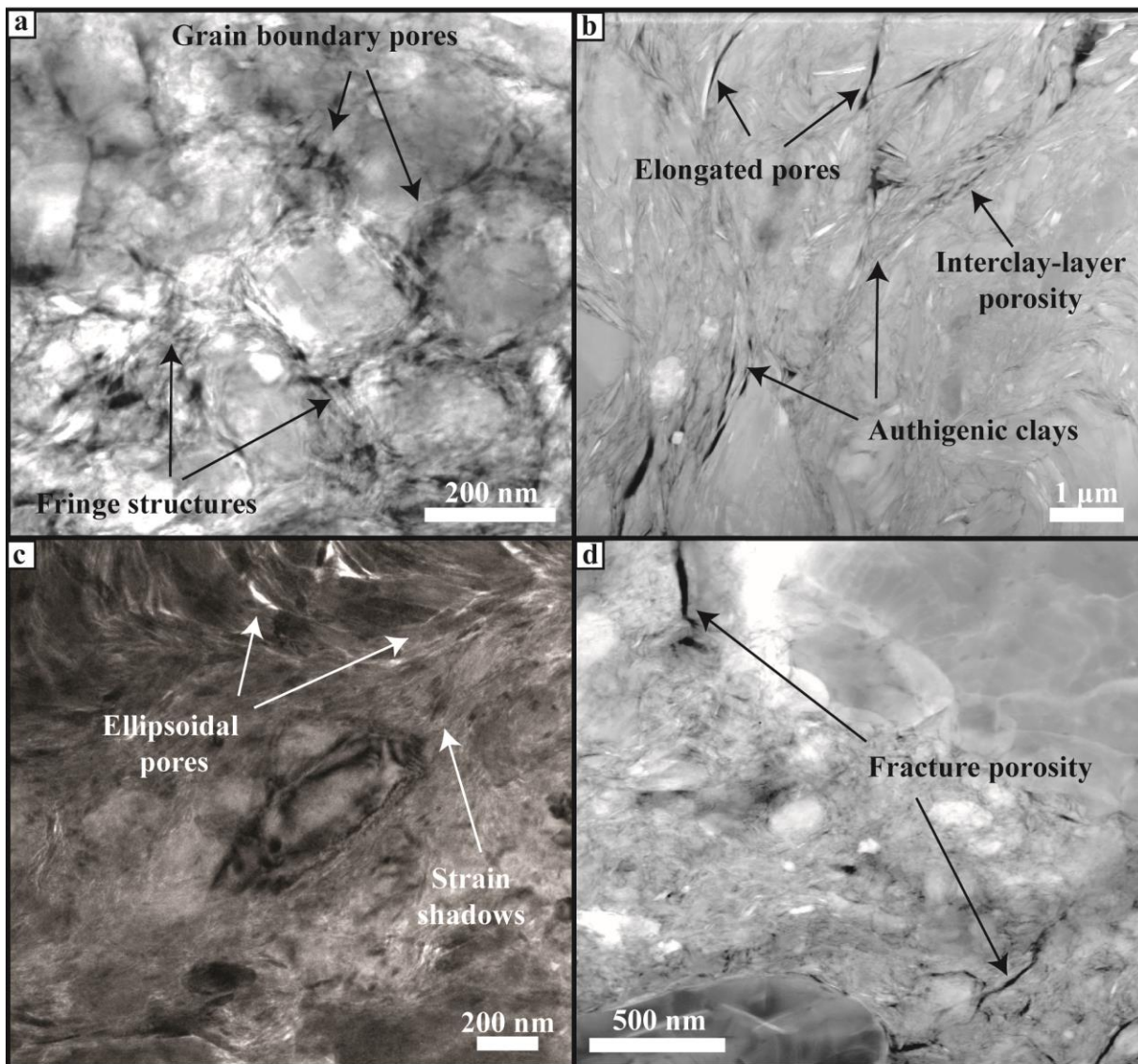
541

542 **Figure 7.** Distribution of pore unit orientations plotted on a lower hemisphere equal area stereographic projection
543 with a probability density contour.



544

545 **Figure 8.** Scanning electron images collected from sample DFDP 1B 69-2.48 showing the existing mineral
 546 associations. (a) Sub-rounded and intensly fractured quartz and white mica clasts in association with white mica.
 547 floating within fine matrix material. (b) Reworked cataclasite clasts in phyllosilicate-rich layermatrix. (c) Fine
 548 chlorite and white mica fillings aggregates in-between quartz clasts. (Qtz = quartz, Wm = white mica, Chl = chlorite).



549

550 **Figure 8Figure 9.** Transmission electron microscopy images collected ~~from~~ from the gouge sample DFDP-1B
 551 69_2.54 (PSZ-2). (a) and (c) are bright-field (BF) images, where porosity appears as bright contrast areas. (b) and
 552 (d) are high-angle annular dark field (HAADF) images, where pores appear as dark contrast areas. (a) TEM bright-
 553 field image of homogeneous fault gouge area. Quartz/feldspar grains, wrapped by fine authigenic clays, displaying
 554 fringe ~~structuresmorphologies~~. Pores with sub-angular shape distributed along grain boundaries. (b) HAADF image
 555 of phyllosilicate-rich gouge area. Co-existence of fine authigenic clays with coarser clay mineral grains. Elongated
 556 pores and interlayer porosity. (c) TEM bright-field image of ellipsoidal pores in phyllosilicate-rich areas. Examples
 557 of strain shadows along quartz/feldspar grains. (d) HAADF image of fracture porosity along grain boundaries of
 558 quartz/feldspar grains.